



Ion Energization and Thermalization in Magnetic Reconnection Exhaust Region in the Solar Wind

Ziqi Wu¹ , Jiansen He¹ , Die Duan¹ , Xingyu Zhu¹ , Chuanpeng Hou¹ , Daniel Verscharen² , Georgios Nicolaou² , Christopher J. Owen² , Andrey Fedorov³ , and Philippe Louarn³

¹ School of Earth and Space Sciences, Peking University, No. 5 Yiheyuan Road, Beijing 100871, People's Republic of China; jshept@pku.edu.cn

² Mullard Space Science Laboratory, University College London, Dorking RH5 6NT, UK

³ Institut de Recherche en Astrophysique et Planétologie, CNRS-UPS-CNES, Toulouse, France

Received 2022 December 3; revised 2023 April 20; accepted 2023 April 21; published 2023 July 6

Abstract

Plasma energization and thermalization in magnetic reconnection is an important topic in astrophysical studies. We select two magnetic reconnection exhausts encountered by Solar Orbiter and analyze the associated ion heating in the kinetic regime. Both cases feature asymmetric plasma merging in the exhaust and anisotropic heating. For a quantitative investigation of the associated complex velocity-space structures, we adopt a three-dimensional Hermite representation of the proton velocity distribution function to produce the distribution of Hermite moments. We also derive the enstrophy and Hermite spectra to analyze the free energy conversion and transfer in phase space. We find a depletion of Hermite power at small m (corresponding to large-scale structures in velocity space) inside the reconnection exhaust region, concurrent with enhanced proton temperature and decreased enstrophy. Furthermore, the slopes of the 1D time-averaged parallel Hermite spectra are lower inside the exhaust and consistent with the effect of phase mixing that creates small fluctuations in velocity space. These fluctuations store free energy at higher m and are smoothed by weak collisionality, leading to irreversible thermalization. We also suggest that the perpendicular heating may happen via perpendicular phase mixing resulting from finite Larmor radius effects around the exhaust boundary.

Unified Astronomy Thesaurus concepts: [Heliosphere \(711\)](#); [Solar magnetic reconnection \(1504\)](#); [Solar wind \(1534\)](#)

1. Introduction

Magnetic reconnection is an important phenomenon in astrophysical and laboratory plasmas. During reconnection, magnetic energy is released and converted into plasma bulk, thermal, or nonthermal kinetic energy through the acceleration of particles or thermalization of the plasma. While plasma heating in magnetic reconnection has been commonly reported in previous studies (Yamada et al. 2010), the details of energy conversion are still not fully understood. Our study focuses on an important aspect of this issue: the ion heating in magnetic reconnection exhausts.

The kinetic physics in the magnetic reconnection diffusion region is essential for the collisionless reconnection events commonly found in space plasmas, which have been studied by hybrid and particle-in-cell (PIC) simulations (Lottermoser et al. 1998; Yin et al. 2001; Lu et al. 2010), as well as observations in Earth's magnetotail and magnetopause (Øieroset et al. 2001; Wang et al. 2010; Zhou et al. 2011; Burch et al. 2016) and in the solar wind (Wang et al. 2022). 2D PIC simulations have shown that the particles in reconnection exhausts follow complicated and dynamic orbits (Zenitani & Nagai 2016), where the mixing of different populations from different trajectories becomes important. Furthermore, kinetic simulations reveal that ions gain an effective thermal speed equal to the exhaust velocity when they cross the boundary and get “picked up” by the accelerated flow in the exhaust region

(Drake et al. 2009). In these situations, the kinetic structures produced in non-Maxwellian velocity distribution functions (VDFs) can compensate for the small collisionality and eventually lead to collisional relaxation and irreversible heating through phase mixing.

Outside the diffusion region and further downstream of the reconnection jet flow, reconnection exhaust regions in the solar wind are often bounded by a slow-shock pair and a rotational-discontinuity pair, characteristic for Petschek-like reconnection (Petschek 1964; Sonnerup 1979; Gosling et al. 2005). In these cases, the exhaust region encountered by spacecraft may be very far away from the ion diffusion region and electron diffusion region where the magnetic reconnection occurs, perhaps more than hundreds of ion inertial lengths in distance. Moreover, the reconnection X-line, which is the intersection of the separatrices between inflow and outflow field topologies, may also extend to great distances (Phan et al. 2006). At large distances from the reconnection site in the reconnection exhaust region, the proton velocity distribution is composed of two field-aligned populations and shaped like a peanut shell or a dumbbell. The velocity difference between the counterstreaming components is of the order of the Alfvén speed. The formation of the counterstreaming dumbbell pattern is related to the deflection and subsequent mixing of the downstream flows in the reference frame of the propagating rotational discontinuities (Gosling et al. 2005; He et al. 2018; Phan et al. 2022). The proton counterstreaming is subject to the firehose instability, which can drive Alfvénic waves propagating from the middle to both sides of the outflow region, contributing to the enhancement of turbulence in the exhaust region (He et al. 2018). Not only do the protons undergo parallel heating due to field-aligned counterstreaming, but the electrons also



Original content from this work may be used under the terms of the [Creative Commons Attribution 4.0 licence](#). Any further distribution of this work must maintain attribution to the author(s) and the title of the work, journal citation and DOI.

undergo evident yet weaker parallel heating. The electron parallel heating leads to a pitch-angle distribution concentrated at 0° and 180° for the superthermal electrons within a certain energy range (He et al. 2018). The enhanced turbulence may cause further diffusion of the non-Maxwellian velocity distribution and relaxation toward the Maxwellian distribution. The observed characteristics of the reconnection exhaust region far away from the reconnection site, including the slow-shock pair, the rotational-discontinuity pair, the dumbbell velocity distribution of protons, etc., have also been reproduced by full kinetic simulations with large simulation domains (Liu et al. 2012; Innocenti et al. 2017).

Phase mixing effects include wave–particle interactions such as Landau damping (Landau 1965) and finite Larmor radius (FLR) induced perpendicular phase mixing (Dorland & Hammett 1993). Particles moving along the magnetic field with a speed close to the propagation speed of the electric field fluctuations are able to resonate with the electric field, resulting in phase mixing, which creates fine phase-space structures in the VDF owing to the mixing of particles from different phase-space locations. This kind of parallel phase mixing and the resultant heating of electrons during wave activity or magnetic reconnection has been studied with kinetic models (Zocco & Schekochihin 2011) and proved to be one of the dominant routes for electron heating (Loureiro et al. 2013). Signatures of field–particle energy transfer have been discovered in Earth’s magnetosheath consistent with Landau damping, suggesting that phase mixing plays a significant role in turbulent plasma heating (Chen et al. 2019). It is also found that kinetic Alfvénic turbulence and compressional turbulence convert electromagnetic field energy by strong dissipation, leading to plasma heating, especially for the electron species in the parallel direction (He et al. 2020). On the other hand, the FLR-corrected electric drift velocity is different for particles with different energy, therefore creating small structures in $f(v_\perp)$ (Dorland & Hammett 1993). We note that the term FLR effects accounts for a multitude of different processes, including phase mixing. Considering the addition of the FLR-related terms to the governing dynamical equations, additional physical effects can be introduced, which are called FLR effects, such as charge separation, particle energization, noncollisional viscous effects, wave dispersion relation corrections, wave instabilities, or dissipation (Stasiewicz 1993). FLR effects play an important role in the heliosphere and in near-Earth space, such as the dissipative heating of the solar wind by turbulence, the interaction between the solar wind and the magnetosphere, the interruption of the magnetotail current sheet, effects related to parallel electric fields, and the electron acceleration that produces the aurora. Energy dissipation related to FLR-induced phase mixing has been studied in electrostatic turbulence (Tatsuno et al. 2009). In collisionless reconnection, gyrokinetic simulations predict that both parallel and perpendicular phase mixing can result in ion heating (Sarto et al. 2011; Numata & Loureiro 2014).

To investigate phase mixing as a dissipation route in phase space, the Hermite representation of the particle VDF can be a helpful approach. The three-dimensional Hermite transformation makes it possible to extract a power-law distribution of moments from complex velocity-space structures. So far, this novel method has been mainly applied to numerical simulation studies, which provide the VDFs with higher velocity-space resolution than spacecraft measurements (Cerri et al. 2018).

The energy conversion and dissipation in Hermite–Fourier space controlled by the coupling of phase mixing and antiphase mixing have been studied in the context of drift-wave turbulence (Schekochihin et al. 2016). Servidio et al. (2017) use a 3D Hermite transformation on the high-resolution measurements from Magnetospheric Multiscale (MMS) in plasma turbulence residing in the magnetosheath. Servidio et al. (2017) derive a $-3/2$ power law of the Hermite spectrum for phase mixing in the unmagnetized regime and a -2 slope for the highly magnetized regime, with the latter supported through the simulation work by Pezzi et al. (2018). However, the role of phase mixing in magnetic reconnection has not yet been investigated in space plasma observations.

In this work, we apply a 3D Hermite transformation to the proton VDF measured by Solar Orbiter during its encounter with two magnetic reconnection exhausts. By comparing the Hermite spectra and other physical properties such as ion temperatures on both sides of the exhaust boundaries, we find signatures of phase mixing in the exhaust and suggest that parallel phase mixing and perpendicular phase mixing play essential roles in the particle thermalization in the reconnection exhaust.

2. Data and Method

2.1. Event Overview

Solar Orbiter, launched in 2020, aims to study the Sun, its outer atmosphere, and the drivers of the constant outflow of solar wind. The Solar Wind Analyser (SWA) suite on the spacecraft consists of an Electron Analyser System (SWA-EAS), a Proton-Alpha Sensor (SWA-PAS), and a Heavy Ion Sensor (SWA-HIS) (Owen et al. 2020). The SWA-PAS instrument is an electrostatic analyzer that measures the full 3D VDF of the protons and alpha particles in the energy range from 200 eV q^{-1} to 20 keV q^{-1} . The SWA-EAS instrument combines two electrostatic analyzer heads (EAS1 and EAS2) to construct the full 3D electron VDF in the energy range from 1 eV to 5 keV. Our study uses the proton VDF data from SWA-PAS, from which we eliminate the alpha population by excluding data points where the phase-space density is less than 1×10^{-8} ($m^{-6} s^3$) and the magnetic field data from the Magnetometer (MAG; Horbury et al. 2020). We also derive the superthermal electron pitch-angle distribution based on the electron data from SWA-EAS. With the observed local magnetic field vector, the coordinates of velocity space are transformed to field-aligned coordinates ($e_\parallel, e_{\perp 1}, e_{\perp 2}$), where $e_{\perp 1}$ is the cross product of the local magnetic field direction and the radial direction of the RTN coordinates, and $e_{\perp 2}$ completes the right-handed reference frame.

Figures 1 and 2 present the two magnetic reconnection exhausts observed by Solar Orbiter on 2021 October 10, 17:19–17:23 UT, and 2021 November 9, 02:41–02:46 UT. Panels (d) and (e) show the vector data transformed into the boundary-normal coordinate system using minimum variance analysis (MVA), where L, M, and N indicate the maximum, intermediate, and minimum variance directions, respectively.

Between 17:19 and 17:23 UT in Case 1, B_L changes sign, and V_L increases while the total magnetic field decreases (Figures 1(d) and (e)), indicating a crossing of a magnetic reconnection exhaust region. An electron dropout occurs in the exhaust bounded by the two black dashed lines. In the exhaust region, B_M first decreases from around 5.5 nT to

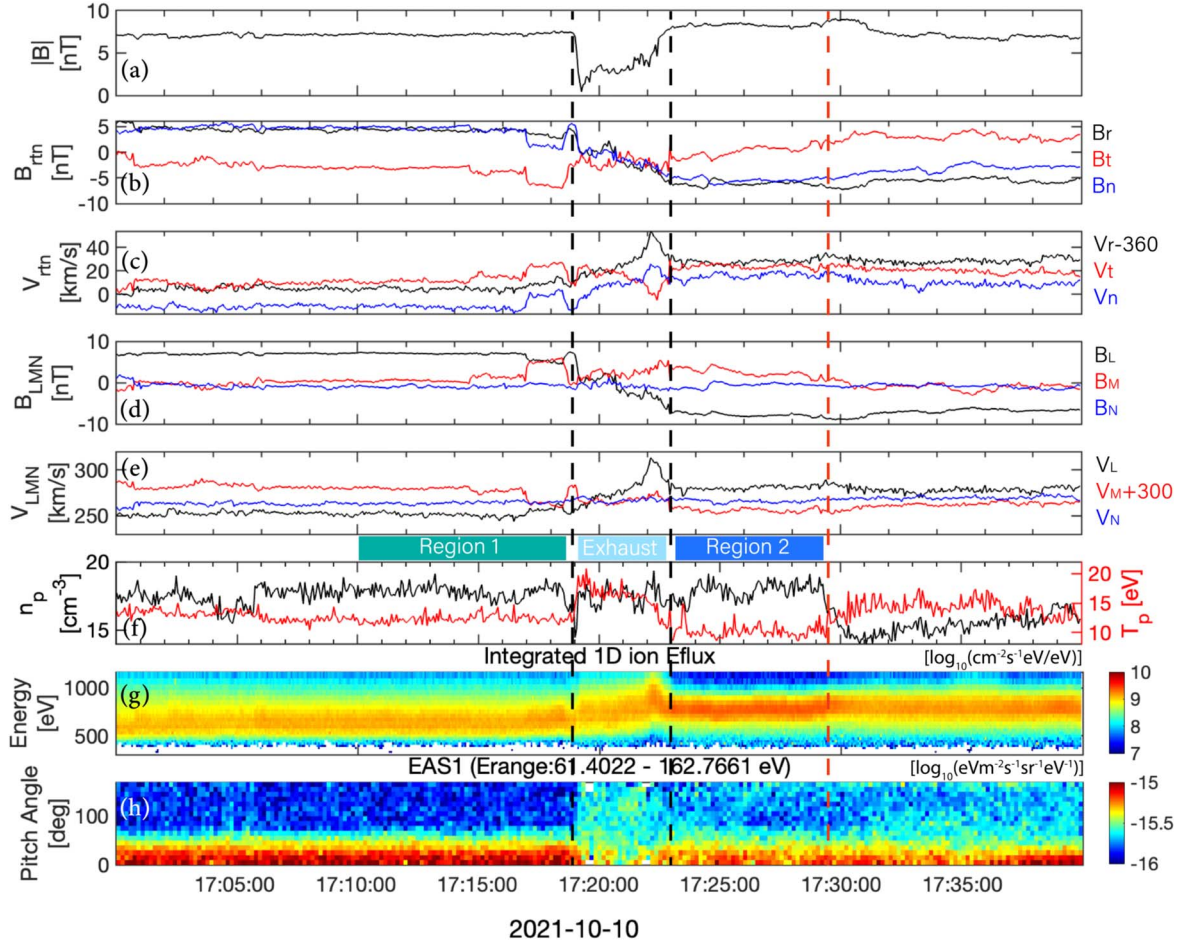


Figure 1. Overview of the magnetic reconnection exhaust encounter on 2021 October 10. (a) The total magnetic field. (b), (c) The three components of the local magnetic field and the bulk velocity in the RTN coordinate system. (d), (e) The three components of the local magnetic field and the bulk velocity in LMN coordinates obtained by MVA analysis. (f) The proton density and temperature. (g) The energy spectrogram of the ions. (h) The pitch-angle distribution of the electrons obtained from EAS1 (Erange:61.4022 - 162.7661 eV). The black dashed lines mark the leading and trailing edges of the exhaust region. The plasma preceding the exhaust region is labeled as Region 1, the plasma in the exhaust is labeled as Exhaust, and the succeeding plasma is labeled as Region 2. The red dashed line marks a candidate contact discontinuity.

around -1.0 nT across the leading edge and then increases to around 5.5 nT at the trailing edge, which is the signature of a guide field modulated by the Hall field (Mistry et al. 2016). We estimate the thickness of the boundary layer by adopting the Harris current sheet model, $B_L(x_N) = B_0 \tanh(x_N/L_t)$, where L_t represents the scale length of the transition layer and the subscripts L and N represent components in the LMN coordinates. We find that $L_t = \left(\frac{dB_L}{dx_N}/B_0\right)^{-1} = \left(\frac{dB_L}{dx_N}/B_0 v_{N'} dt\right)^{-1}$, where $v_{N'} = v_{SW,N} - v_{sc,N}$ is the relative speed between the spacecraft and the solar wind and dt is the crossing time. The thickness of the transition layers is 1981 km at the leading edge and 4954 km at the trailing edge. The relatively sharp decrease in B_M at the exhaust boundary suggests perpendicular ion heating due to the violation of the magnetic moment when particles enter the exhaust and get “picked up” by the fast-convected reconnected magnetic field (Drake et al. 2009).

The ambient plasma preceding and succeeding the exhaust region (marked as Region 1 and Region 2 in Figure 1) shows a significant asymmetry. Plasma in Region 1 has a lower bulk velocity V_r , a slightly higher temperature, but a similar proton density compared to the plasma in Region 2. In addition, the energy spectrum of the ion flux in Region 2 is narrower, with higher flux in the center part of the energy distribution. In the exhaust region, the merged plasma is energized and heated as

indicated by the lifted and expanded ion flux spectrum. The red dashed line succeeding Region 2 marks potentially a contact discontinuity, across which the plasma becomes sparser and hotter.

Case 2 shows similar magnetic reconnection exhaust characteristics to Case 1 between 02:41 and 02:46 UT (Figure 2), such as the anticorrelated V_L and B_L at the leading and trailing edges of the exhaust, as well as the electron dropout. There is also a nonzero guide field, B_M , in the reconnection exhaust, but weaker than in Case 1. The thickness of the transition layers is 1162 km at the leading edge and 2324 km at the trailing edge. Regarding the plasma properties in Case 2, the plasma in Region 1 preceding the exhaust has a lower density, a slightly higher temperature, and a lower bulk velocity compared to Region 2. Ions are energized and heated in the exhaust, but the temperature enhancement is lower than in Case 1. While there is no apparent discontinuity, the Region 2 plasma can also be distinguished from the following region by its centralized energy spectrum and low temperature.

2.2. Hermite Transformation

The Hermite transformation is introduced to help analyze free energy conversion and transport in the kinetic regime inside the exhaust. Analogous to the Fourier transformation

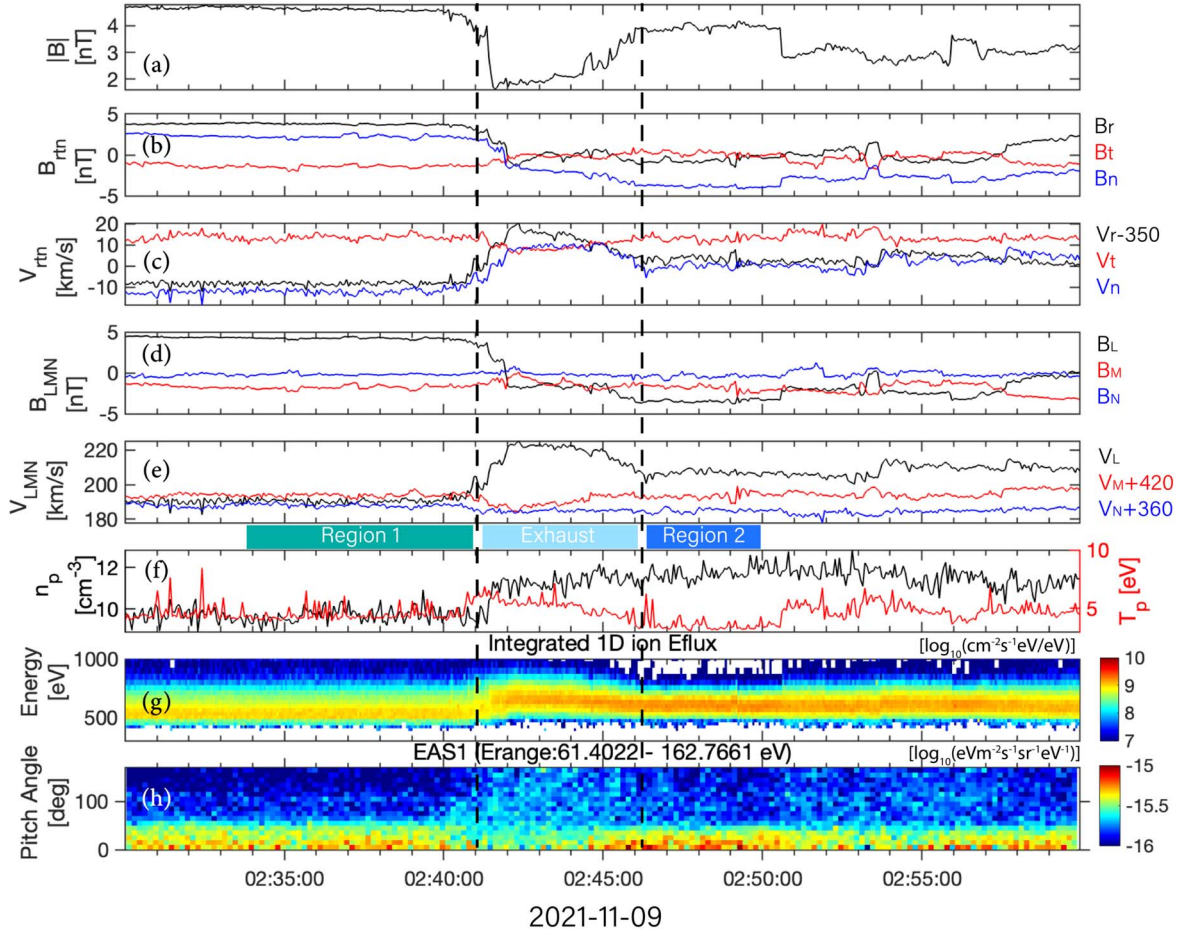


Figure 2. Overview of the magnetic reconnection exhaust encounter on 2021 November 9. The format is the same as in Figure 1.

that projects signals from the time domain into the frequency domain, the Hermite transformation provides a method for us to analyze the structures of the proton VDF in Hermite space.

We expand the proton VDF, $f(v, t)$, in terms of Hermite polynomials in magnetic-field-aligned coordinates. The relevant 1D basis functions are

$$\psi_m(v) = \frac{H_m\left(\frac{v-u}{v_{\text{th}}}\right)}{\sqrt{2^m m!} \sqrt{\pi} v_{\text{th}}} e^{-(v-u)^2/2v_{\text{th}}^2}, \quad (1)$$

where u and v_{th} are the bulk velocity and the thermal velocity, respectively, derived from integrals of the proton VDF. The ‘‘Physicist’s’’ Hermite polynomials are defined as $H_m(v) = (-1)^m e^{v^2} (d^m/dv^m) e^{-v^2}$, with m being an integer designated as the Hermite index. The basis functions meet the orthogonality condition $\int_{-\infty}^{\infty} \psi_m(v) \psi_l(v) dv = \delta_{ml}$. This property allows us to decompose the 3D VDF into a set of Hermite coefficients in 3D Hermite phase space:

$$f(\mathbf{v}) = \sum_{m=0}^M f_m \psi_m(\mathbf{v}), \quad (2)$$

where \mathbf{m} refers to (m_x, m_y, m_z) and the 3D basis function is defined as $\psi_{\mathbf{m}}(\mathbf{v}) = \psi(m_x, v_x) \psi(m_y, v_y) \psi(m_z, v_z)$. The

resultant Hermite coefficients are

$$f_m = \int_{-\infty}^{\infty} f(\mathbf{v}) \psi_m(\mathbf{v}) d^3v. \quad (3)$$

First, we perform interpolation and normalization on the data before applying the Hermite transformation. A ‘‘Hermite grid’’ is adopted to improve accuracy since it naturally allows Gauss–Hermite quadrature during the integration. The Hermite grid is a 3D nonuniform grid in which the roots of the $(M+1)$ th Hermite polynomial act as nodes in all three dimensions. In our study, we choose $M=50$ as the maximum order of the transformation, and therefore our grid resolution is $(51 \times 51 \times 51)$. Here the choice of M is mainly limited by the resolution of spacecraft measurements. For normalization, we first subtract the local bulk velocity vector from the velocity-space coordinates and then normalize all velocities in units of the local thermal velocity as defined in Equation (1). The number density is normalized such that $n=1$. As a result, the procedure above produces a normalized VDF on the nonuniform Hermite grid.

In principle, the Hermite transformation applies to distribution functions independently of the applied normalization factors. However, by normalizing the measured VDF with the local bulk velocity and the local thermal velocity, we examine the local deviations from the Maxwellian distribution and gain a hierarchy of Hermite coefficients that resembles the moment hierarchy of the velocity distribution. The same normalizing technique has also been adopted by Servidio et al. (2017) to

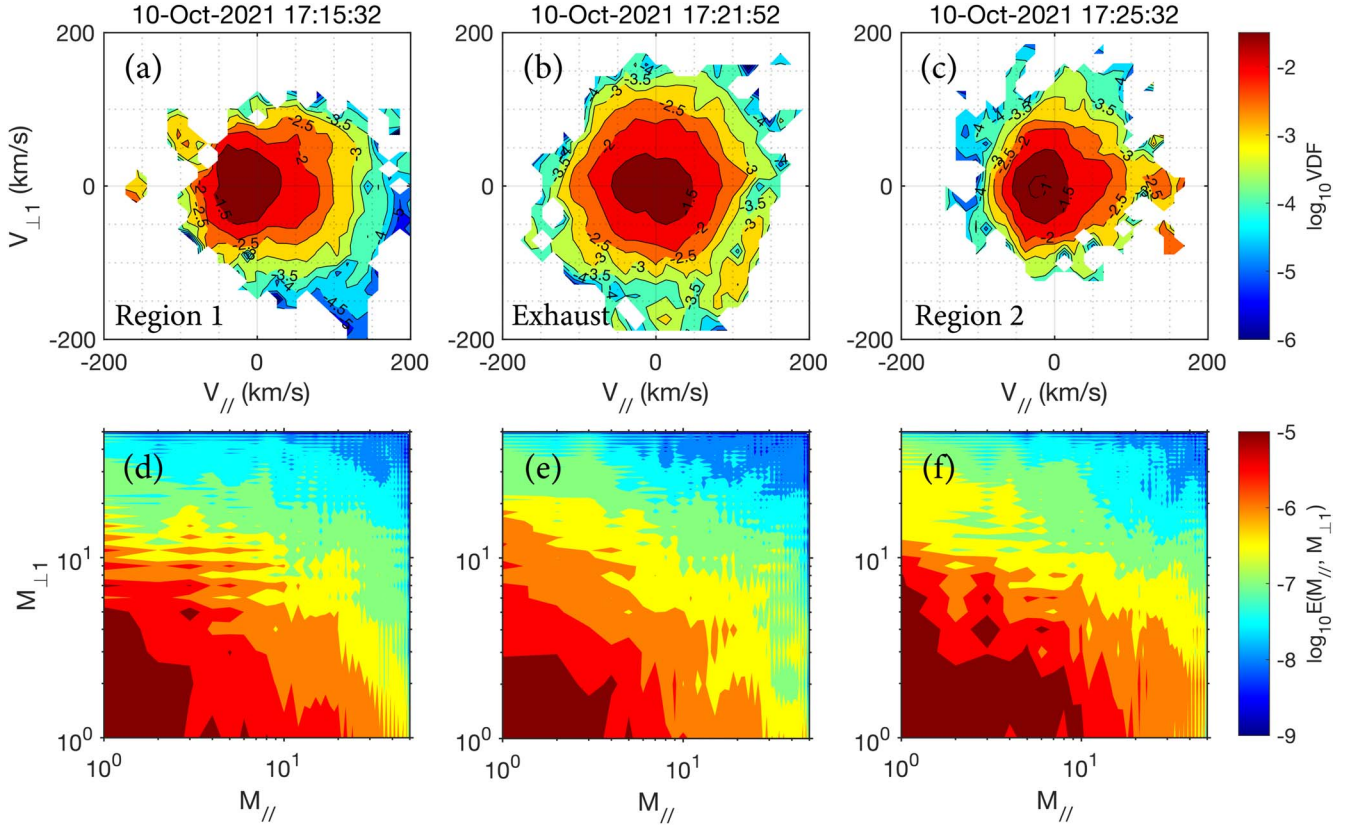


Figure 3. Cuts of the proton VDFs and the 2D Hermite spectra for Case 1. The first row shows the VDF cuts in the $(V_{||}, V_{\perp})$ -plane, and the second row shows the corresponding 2D Hermite spectra calculated from the Hermite coefficient distribution. The three columns are extracted from Region 1, the exhaust, and Region 2, respectively.

analyze measurements from MMS, where the velocity distributions are not necessarily close to a Maxwellian equilibrium. Since the nonthermal fraction of the VDF can potentially influence the integrated normalization parameters u and v_{th} , we fit the proton VDF to a two-component Gaussian model and vary the thermal speed in the normalization. We apply the thermal speed based on the full VDF (core and beam) and the thermal speed based on the core part only. The results show that the influence of the nonthermal fraction is negligible for plasma inside the exhaust.

Based on the normalized VDF, we calculate the Hermite coefficients (f_{mx}, f_{my}, f_{mz}) according to Equation (3). Here x , y , and z represent $e_{||}$, $e_{\perp 1} = e_b \times e_R$, and $e_{\perp 2} = e_b \times e_{\perp 1}$, respectively. The m th coefficient is a measure for structures in the VDF, with higher m corresponding to smaller scales in velocity space. With the recursion relations

$$\begin{aligned} v\psi_m(v) &= \sqrt{\frac{m}{2}}\psi_{m-1}(v) + \sqrt{\frac{m+1}{2}}\psi_{m+1}(v) \\ \frac{\partial\psi_m(v)}{\partial v} &= \sqrt{\frac{m}{2}}\psi_{m-1}(v) - \sqrt{\frac{m+1}{2}}\psi_{m+1}(v) \end{aligned} \quad (4)$$

the collisionless Vlasov equation (Equation (5)) can be transformed into a set of coupled equations of $\frac{\partial}{\partial r}f_m(\mathbf{x}, t)$ (Equation (6)):

$$\frac{\partial f}{\partial t} + \nabla \cdot (vf) + \frac{e}{M_p} \left(\mathbf{E} + \frac{\mathbf{v}}{c} \times \mathbf{B} \right) \cdot \nabla_v f = 0 \quad (5)$$

$$\begin{aligned} \frac{\partial f_m}{\partial t} + \nabla \cdot \left(\sqrt{\frac{m+1}{2}} f_{m+1} + \sqrt{\frac{m}{2}} f_{m-1} \right) \\ + \frac{e}{M_p} \left(\mathbf{E} + \frac{\mathbf{v}}{c} \times \mathbf{B} \right) \cdot \left(\sqrt{\frac{m+1}{2}} f_{m+1} - \sqrt{\frac{m}{2}} f_{m-1} \right) = 0. \end{aligned} \quad (6)$$

The fact that the m th Hermite coefficient couples to both the $(m-1)$ th and $(m+1)$ th coefficients indicates the dynamic transfer between different orders of moments. In the work presented by Schekochihin et al. (2016), linear phase mixing, which transfers free energy from lower m to higher m , competes against nonlinear advection, another physical process that diverts free energy into a cascade toward finer spatial scales. For weakly collisional plasmas, linear phase mixing provides a route for free energy to cascade in velocity space and finally convert into heat irreversibly. To this end, we adopt the concept of “enstrophy,” the second Casimir invariant of the VDF, to quantify its local deviation from the Maxwellian distribution. Enstrophy Ω is defined as

$$\Omega(t) \equiv \int_{-\infty}^{\infty} \delta f^2(v, t) d^3v = \sum_{m>0} [f_m(t)]^2, \quad (7)$$

where $\delta f = f(v) - M(v)$. We adopt Parseval’s theorem to convert the integration to the sum of squared Hermite coefficients. In certain reduced perturbative treatments of kinetic plasmas, enstrophy is analogous to the idea of “free energy” (Servidio et al. 2017; Pezzi et al. 2018).

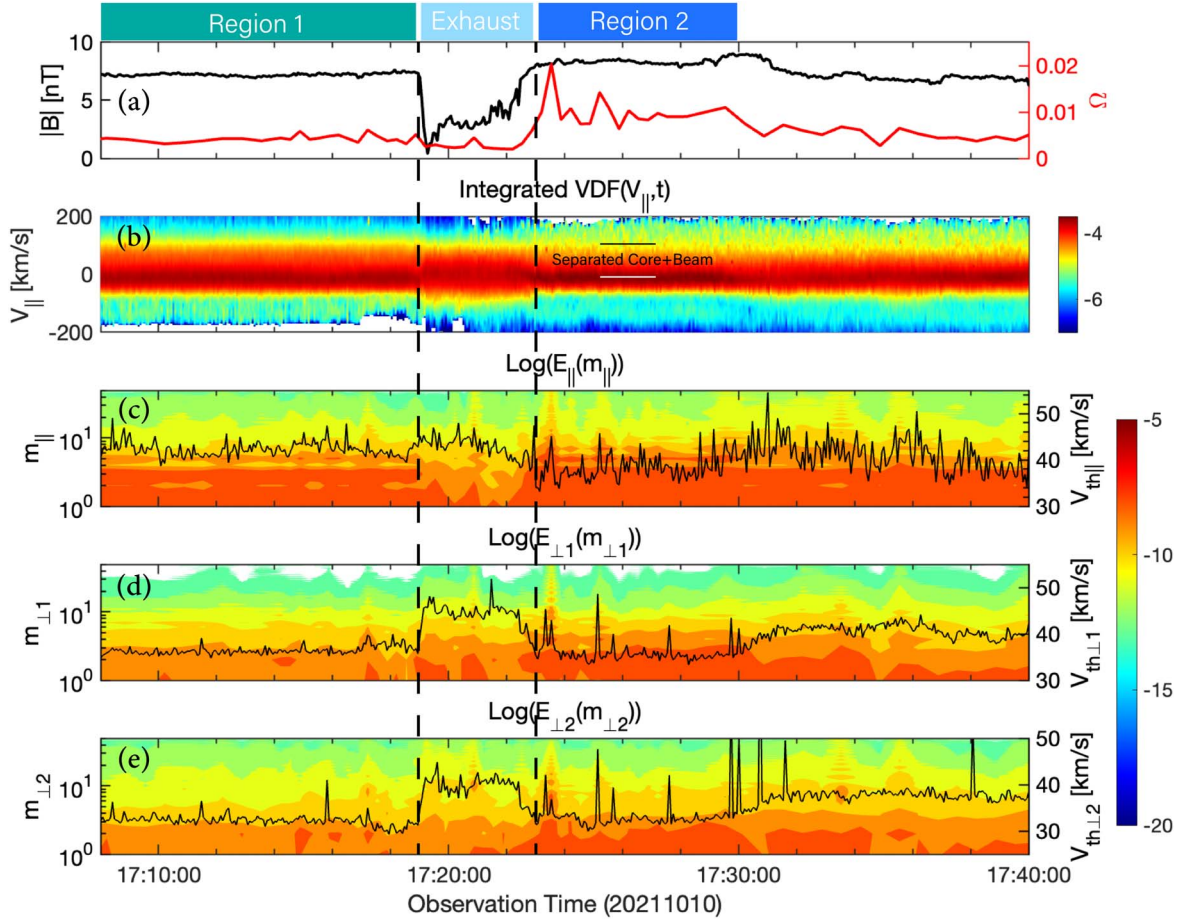


Figure 4. 1D Hermite spectra for Case 1. (a) The total magnetic field and enstrophy. (b) The integrated VDF along the parallel direction. (c)–(e) The reduced 1D Hermite spectra along and across the local magnetic field, where $e_{\perp 1} = e_b \times e_R$, $e_{\perp 2} = e_b \times e_{\perp 1}$. The black dashed lines mark the leading and trailing edges of the magnetic reconnection exhaust.

Around the exhaust boundary, FLR effects become important, since the scale length of the particle motion becomes comparable to the width of the exhaust boundary layers. The divergence of drift motions leads to perpendicular phase mixing that creates fluctuations in velocity space. FLR-induced phase mixing may result in a hyperviscosity-like damping process (Dorland & Hammett 1993; Numata & Loureiro 2014).

3. Results

Following the algorithm described in Section 2, we compute the 3D Hermite coefficients as $f(m_{\parallel}, m_{\perp 1}, m_{\perp 2}, t)$. The full 3D Hermite spectrum is therefore defined as $E(\mathbf{m}, t) = f(\mathbf{m}, t)^2$.

We visualize the features of the coefficient distribution in Hermite space by summing up the coefficients along one of the three dimensions, leading to reduced 2D spectra that are defined as $E(m_{\parallel}, m_{\perp 1}) = \sum_{m_{\perp 2}} E(\mathbf{m}, t)$, etc. In Figure 3, we present cuts of the proton VDFs and the corresponding 2D Hermite spectra extracted from the three regions in Case 1. Figures 3(a) and (c) show that the proton VDFs in Region 1 and Region 2 possess a core+beam structure. The beam population moves along the local magnetic field, flowing toward the exhaust region. Figure 3(b) shows that in the exhaust region the proton VDF has two merging components that are similar to each other, resulting in a peanut-shell-like distribution, which represents the counterstreaming of plasma in the exhaust region. The 2D Hermite spectra in Figures 3(d)–

(f) show features that agree with the proton VDF. In Region 1 and Region 2, the Hermite spectra are extended in the direction parallel to the local magnetic field and therefore aligned with the drifting beam. In the exhaust region, the 2D Hermite spectra are suppressed along the local magnetic field.

We then obtain the 1D reduced Hermite spectra along each dimension separately to examine their variation over time. In an analogous manner to the 2D reduced Hermite spectra, these 1D reduced spectra are defined as $E_{\parallel}(m_{\parallel}, t) = \sum_{m_{\perp 1}} \sum_{m_{\perp 2}} E(\mathbf{m}, t)$, etc. We also compute the enstrophy as a function of time to evaluate the non-Maxwellianity of the proton VDF. The results for Case 1 and Case 2 are shown in Figures 4 and 5, respectively. Figure 4(b) shows the merging of ions from Region 1 and Region 2 in the reconnection exhaust of Case 1. As shown in Figure 3, the proton VDFs in Region 1 and Region 2 possess a field-aligned beam, and the core and beam are more separated in Region 2. In the exhaust, the merged proton VDF shows an extended core population along the local magnetic field direction (seen as the broadened dark red stripe in Figures 4(b) and 5). The enstrophy is also lower in the exhaust, indicating that the proton VDF is more Maxwellian owing to merging and possibly stronger collisionality. As shown by the time series of thermal velocity, the proton heating is anisotropic, with weak parallel heating and significant perpendicular heating. Similar features can also be found in Case 2.

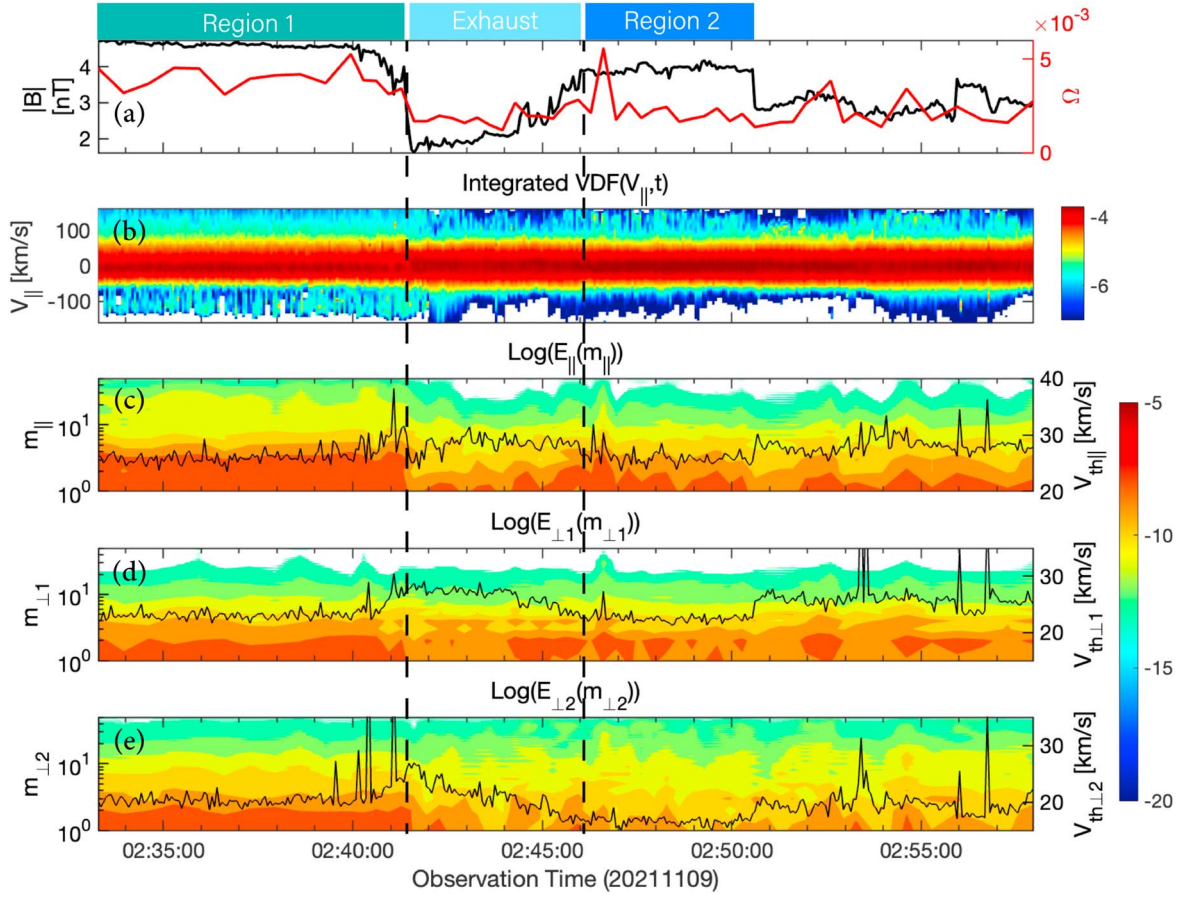


Figure 5. 1D Hermite spectra for Case 2. The format is the same as in Figure 4.

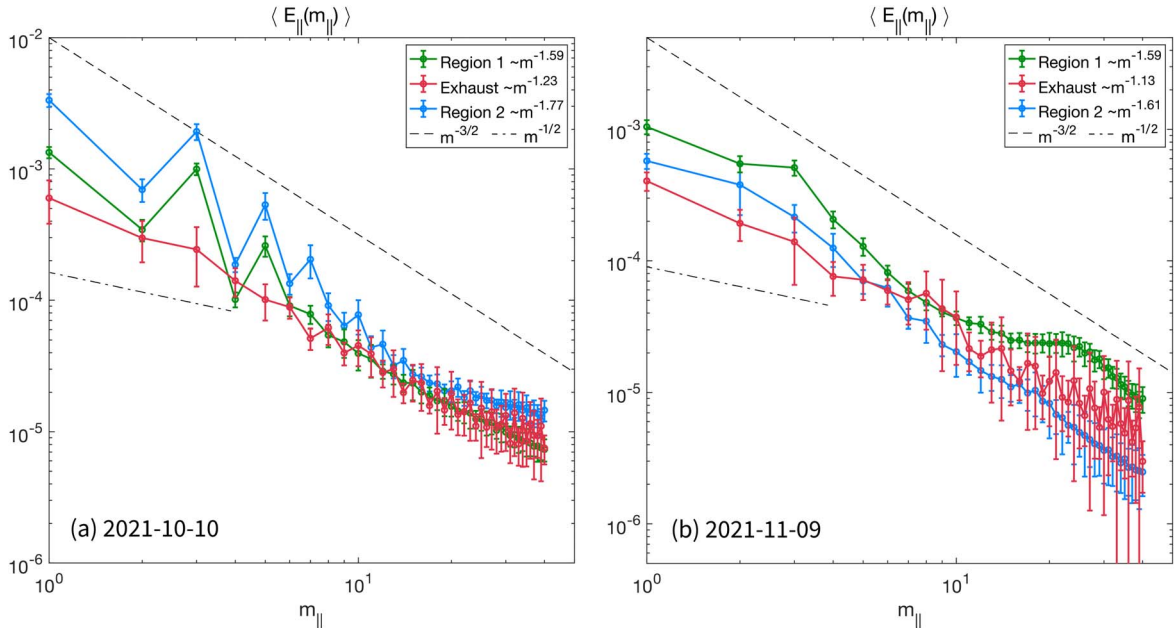


Figure 6. 1D Hermite spectra averaged in Region 1, Region 2, and the exhaust region on (a) 2021 October 10 for Case 1 and (b) 2021 November 9 for Case 2. The green, blue, and red lines denote Region 1, Region 2, and the exhaust region, respectively. The black dashed reference lines indicate an $m^{-3/2}$ slope, and the black dotted–dashed lines indicate an $m^{-1/2}$ slope. The slopes listed in the legend are calculated by fitting the first 12 moments of the Hermite spectra.

Turning to the reduced 1D Hermite spectra, in the parallel direction, we find a depletion of the Hermite power at lower m inside the exhaust, coinciding with the low-entropy trough in both Case 1 and Case 2. In the perpendicular directions, the

spectral depletion at lower m is less significant, while the thermal velocity enhancements are greater than the parallel ones. The spectral depletion at lower m is consistent with phase mixing in the exhaust, with the free energy in the weakly

Table 1

The Boundary Layer Scale Length L_t , the Pickup Parameter ε_p , and the FLR Parameter ε_{th} for the Edges of the Exhausts

		L_t (km)	$\varepsilon_p = v_{HT}/(\Omega_p L_t)$	$\varepsilon_{th} = R_{th}/L_t$
Case 1	Leading	1981	4.78	0.42
	Trailing	4954	0.18	0.02
Case 2	Leading	1162	1.83	0.13
	Trailing	2324	0.59	0.03

collisional non-Maxwellian VDF being transported to higher m .

Finally, we compare the 1D Hermite spectra averaged in Region 1, Region 2, and the exhaust region (Figure 6). We calculate the slopes by fitting the first 12 moments of the Hermite spectra. Since the proton VDF in our cases is anisotropic, we calculate the 1D spectra along the local magnetic field instead of the isotropic Hermite spectra calculated by Servidio et al. (2017). In both cases, the spectra inside the exhaust are lower at the first three moments and possess a flatter slope around $m^{-1.13-1.23}$. The spectra of the inflow regions are higher at low m and have a steeper slope around $m^{-1.59-1.77}$.

4. Summary and Discussion

We investigate the energy conversion and plasma heating in the weakly collisional magnetic reconnection exhausts encountered by Solar Orbiter on 2021 October 10 (0.68 au) and 2021 November 9 (0.88 au). The two magnetic reconnection cases are characterized by asymmetric plasma upstream, which is merged and heated in the exhaust. The protons upstream exhibit field-aligned beams in velocity space, while the proton VDF downstream shows a peanut-shell-like distribution at its inner part and is more isotropic and Maxwellian at its outer part. A 3D Hermite transformation allows us to analyze the distribution of moments in Hermite space. As expected from the observed proton VDF, the reduced 2D Hermite spectra are more extended in the parallel direction outside the exhaust than inside the exhaust owing to the drifting beam population.

Furthermore, the ion heating in the exhaust is anisotropic, with more perpendicular than parallel heating. In the parallel direction, the core+beam structure in the upstream proton VDF leads to a high value of the parallel thermal speed. However, the merged VDF inside the exhaust is more Maxwellian, therefore possessing less free energy. Previous studies usually find intense parallel heating in the exhaust as a result of counterstreaming, where Maxwellian proton VDFs from the upstream regions on both sides merge to form a dumbbell distribution (Drake et al. 2009; He et al. 2018). However, in our cases, the upstream proton VDF already consists of a distinctive core+beam structure. During the merging inside the exhaust, phase mixing smooths out irregularities and thermalizes the plasma, leading to more Maxwellian VDFs inside the exhaust.

To clarify the cause of the observed perpendicular heating, we examine the criteria for FLR effects and the pickup mechanism by comparing the scale length for particle motion with the width of the exhaust boundary layers L_t . We calculate the parameter $\varepsilon = R_H/L_t$ to examine FLR effects. R_H is the proton Larmor radius given by $R_H = v_{th,\perp}/\Omega_p$, where Ω_p is the

proton gyrofrequency and $v_{th,\perp}$ is the perpendicular thermal speed. According to Stasiewicz (1993), $\varepsilon > 1$ indicates the existence of significant FLR effects, while in a Harris current sheet model $\varepsilon \approx 1$ indicates stochastic heating by the chaotic motion of particles. We also calculate the pickup parameter $\varepsilon_p = v_{HT}/(\Omega_p L_t)$, where v_{HT} is the de Hoffman–Teller velocity. According to Drake et al. (2009), the pickup regime is characterized by $\varepsilon_p > 1$. The calculated parameters for our cases are shown in Table 1. We find that the pickup criterion is satisfied at the leading edges in both cases and that FLR effects are nonnegligible at the leading edges. The asymmetry of these parameters reflects the asymmetric heating at the leading and trailing edges, which naturally arises from the different widths of the transition layers. The effects of other heating mechanisms, like Fermi or betatron heating, cannot be ruled out; however, their evaluation based on single-point measurements is very uncertain. Future studies of this kind using MMS data may allow us to assess the contributions of the different heating mechanisms.

In the moment hierarchy derived from the Hermite transformation, we find signatures of parallel phase mixing inside the exhaust, such as power depletion in the 1D reduced Hermite spectra at lower m , low enstrophy, and -1.13 to -1.23 slopes of the averaged 1D Hermite spectra. In former studies, Servidio et al. (2017) deduce a $-3/2$ power law for phase mixing or an electric-field-dominant regime and a -2 power law for highly magnetized plasma, obtained by summing the Hermite coefficients over concentric shells to acquire isotropic Hermite spectra. Pezzi et al. (2018) confirm the latter power law in magnetized plasma through numerical simulations in both isotropic and parallel spectra. The parallel Hermite spectrum derived by Cerri et al. (2018) possesses a $-1/2$ power law for $m < 15$ and a $-3/2$ power law for higher m . The $-1/2$ spectrum likely reflects the linear phase mixing parallel to the magnetic field as predicted by Zocco & Schekochihin (2011). The 1D parallel spectra in our work are derived differently from the isotropic spectrum analyzed by Servidio et al. (2017), which does not account for anisotropy in velocity space. However, our method is similar to the approach chosen by Cerri et al. (2018). Likewise, we find Hermite-spectral slopes close to $-1/2$ at lower m and $-3/2$ at higher m , consistent with the occurrence of phase mixing. The weak collisionality of the ion VDF may be responsible for eventually dissipating the free energy stored in finer-scale structures in velocity space, accounting for the steeper spectra at large m .

Ion heating, defined by the enhancement of the second velocity moment integrated from the proton VDF, is not necessarily an irreversible process. On the other hand, energy dissipation, defined as entropy production or free energy loss, is an irreversible process in which collisions must participate. In our cases, the parallel thermal speed shows a slight enhancement across the exhaust boundary. However, the enstrophy (free energy) is significantly lower in the exhaust region. We suggest that the free energy stored in velocity space cascades through phase mixing toward higher Hermite moments, creating even smaller-scale fluctuations in velocity space, and is finally converted into heat irreversibly through weak collisions. Therefore, the proton VDF inside the exhaust is more Maxwellian and possesses lower enstrophy and thus higher entropy (Schekochihin et al. 2016).

In summary, we use the novel technique of Hermite transformation to comprehensively investigate the energy

conversion in velocity space. Our findings highlight the importance of parallel and perpendicular phase mixing in the heating and thermalization of weakly collisional plasma. Using VDF data measured by Solar Orbiter SWA-PAS, we expand the application of Hermite transformations to observations. While the limited data resolution in velocity space leads to restricted Hermite indexes in the transformation, the Hermite spectra for Hermite coefficients below 40 successfully indicate signatures of phase mixing. Future work involving kinetic simulations will further improve our understanding of the free energy cascade and transfer in both velocity and configuration space.

Acknowledgments

The work at Peking University is supported by NSFC (42241118, 42174194, 42150105, and 42204166), by CNSA (D050106), and by the National Key R&D Program of China (2021YFA0718600 and 2022YFF0503800). D.V., G.N., and C.O. from UCL are supported by STFC Consolidated Grants ST/S000240/1 and ST/W001004/1. D.V. is also supported by STFC Ernest Rutherford Fellowship ST/P003826/1. Z.Q. W. is also supported by the National Innovation Training Program for Undergraduates. D.D. is also funded by China Postdoctoral Science Foundation (2022M720213). Solar Orbiter is a space mission of international collaboration between ESA and NASA, operated by ESA. We thank the entire Solar Orbiter team and the instrument PIs for data access and support. Solar Orbiter data are available at <http://soar.esac.esa.int/soar/#home>. Solar Orbiter magnetometer operations are funded by the UK Space Agency (grant ST/T001062/1). Solar Orbiter Solar Wind Analyser (SWA) data are derived from scientific sensors that have been designed and created and are operated under funding provided in numerous contracts from the UK Space Agency (UKSA), the UK Science and Technology Facilities Council (STFC), with operations currently funded under grant ST/X002152/1, the Agenzia Spaziale Italiana (ASI), the Centre National d'Etudes Spatiales (CNES, France), the Centre National de la Recherche Scientifique (CNRS, France), the Czech contribution to the ESA PRODEX program, and NASA.

ORCID iDs

Ziqi Wu  <https://orcid.org/0000-0002-1349-8720>
 Jiansen He  <https://orcid.org/0000-0001-8179-417X>
 Die Duan  <https://orcid.org/0000-0002-6300-6800>
 Xingyu Zhu  <https://orcid.org/0000-0002-1541-6397>

Chuanpeng Hou  <https://orcid.org/0000-0001-7205-2449>
 Daniel Verscharen  <https://orcid.org/0000-0002-0497-1096>
 Georgios Nicolaou  <https://orcid.org/0000-0003-3623-4928>
 Christopher J. Owen  <https://orcid.org/0000-0002-5982-4667>
 Andrey Fedorov  <https://orcid.org/0000-0002-9975-0148>
 Philippe Louarn  <https://orcid.org/0000-0003-2783-0808>

References

- Burch, J., Torbert, R., Phan, T., et al. 2016, *Sci*, **352**, aaf2939
 Cerri, S. S., Kunz, M. W., & Califano, F. 2018, *ApJL*, **856**, L13
 Chen, C. H. K., Klein, K. G., & Howes, G. G. 2019, *NatCo*, **10**, 740
 Dorland, W., & Hammett, G. W. 1993, *PhFIB*, **5**, 812
 Drake, J. F., Swisdak, M., Phan, T. D., et al. 2009, *JGRA*, **114**, A05111
 Gosling, J., Skoug, R., McComas, D., & Smith, C. 2005, *JGRA*, **110**, A01107
 He, J., Zhu, X., Verscharen, D., et al. 2020, *ApJ*, **898**, 43
 Horbury, T. S., O'Brien, H., Carrasco Blazquez, I., et al. 2020, *A&A*, **642**, A9
 Innocenti, M. E., Cazzola, E., Mistry, R., et al. 2017, *GeoRL*, **44**, 3447
 He, J., Zhu, X., Chen, Y., et al. 2018, *ApJ*, **856**, 148
 Landau, L. D. 1965, in *Collected Papers of L. D. Landau*, ed. D. Ter Haar (Amsterdam: Elsevier), 445
 Liu, Y.-H., Drake, J., & Swisdak, M. 2012, *PhPI*, **19**, 022110
 Lottermoser, R.-F., Scholer, M., & Matthews, A. P. 1998, *JGRA*, **103**, 4547
 Loureiro, N. F., Schekochihin, A. A., & Zocco, A. 2013, *PhRvL*, **111**, 025002
 Lu, Q., Huang, C., Xie, J., et al. 2010, *JGRA*, **115**, A11208
 Mistry, R., Eastwood, J. P., Haggerty, C. C., et al. 2016, *PhRvL*, **117**, 185102
 Numata, R., & Loureiro, N. F. 2014, *JPIPh*, **81**, 305810201
 Øieroset, M., Phan, T. D., Fujimoto, M., Lin, R. P., & Lepping, R. P. 2001, *Natur*, **412**, 414
 Owen, C. J., Bruno, R., Livi, S., et al. 2020, *A&A*, **642**, A16
 Petschek, H. E. 1964, *NASSP*, **50**, 425
 Pezzi, O., Servidio, S., Perrone, D., et al. 2018, *PhPI*, **25**, 060704
 Phan, T., Gosling, J., Davis, M., et al. 2006, *Natur*, **439**, 175
 Phan, T., Verniero, J., Larson, D., et al. 2022, *GeoRL*, **49**, e96986
 Sarto, D. D., Marchetto, C., Pegoraro, F., & Califano, F. 2011, *PPCF*, **53**, 035008
 Schekochihin, A. A., Parker, J. T., Highcock, E. G., et al. 2016, *JPIPh*, **82**, 905820212
 Servidio, S., Chasapis, A., Matthaeus, W., et al. 2017, *PhRvL*, **119**, 205101
 Sonnerup, B. U. Ö. 1979, *Space Plasma Physics: The Study of Solar-System Plasmas*, Vol. 2 (Washington, DC: National Academy Sciences), 879
 Stasiewicz, K. 1993, *SSRv*, **65**, 221
 Tatsuno, T., Dorland, W., Schekochihin, A. A., et al. 2009, *PhRvL*, **103**, 015003
 Wang, R., Lu, Q., Huang, C., & Wang, S. 2010, *JGRA*, **115**, A01209
 Wang, R., Wang, S., Lu, Q., et al. 2023, *NatAs*, **7**, 18
 Yamada, M., Kulsrud, R., & Ji, H. 2010, *RvMP*, **82**, 603
 Yin, L., Winske, D., Gary, S. P., & Birn, J. 2001, *JGR*, **106**, 10761
 Zenitani, S., & Nagai, T. 2016, *PhPI*, **23**, 102102
 Zhou, M., Pang, Y., Deng, X. H., Yuan, Z. G., & Huang, S. Y. 2011, *JGRA*, **116**, A06222
 Zocco, A., & Schekochihin, A. A. 2011, *PhPI*, **18**, 102309